

Long range absorption in the scattering of ${}^6\text{He}$ on ${}^{208}\text{Pb}$ and ${}^{197}\text{Au}$ at 27 MeV.

O. R. Kakuee^{a,c}, M. A. G. Alvarez^c, M. V. Andrés^c, S. Cherubini^{d,f}, T. Davinson^b, A. Di Pietro^b, W. Galster^d, J. Gómez-Camacho^c, A. M. Laird^b, M. Laméhi-Rachti^a, I. Martel^e, A. M. Moro^c, J. Rahighi^{a,b}, A. M. Sánchez-Benitez^e, A. C. Shotter^b, W. B. Smith^b, J. Vervier^d, P. J. Woods^b.

^aVan De Graaf Laboratory, Nuclear Research Centre, AEOI, P. O. Box 14155-1339, Tehran, Iran

^bDepartment of Physics and Astronomy, Edinburgh University EH9 3JZ, UK

^cDepartamento de Física Atómica, Molecular y Nuclear,
Apartado 1065, Universidad de Sevilla, E-41080 Sevilla, Spain

^dDepartment de Physique Nucleaire, Université Catholique, Louvain-la-Neuve, Belgium

^eDepartamento de Física Aplicada, Universidad de Huelva, E-21819, Huelva, Spain and

^fInstitut für Experimentalphysik III, Ruhr-Universität Bochum, Germany.

(Dated: November 8, 2018)

Quasi-elastic scattering of ${}^6\text{He}$ at $E_{\text{lab}}=27$ MeV from ${}^{197}\text{Au}$ has been measured in the angular range of $6^\circ - 72^\circ$ in the laboratory system employing LEDA and LAMP detection systems. These data, along previously analysed data of ${}^6\text{He} + {}^{208}\text{Pb}$ at the same energy, are analysed using Optical Model calculations. The role of Coulomb dipole polarizability has been investigated. Large imaginary diffuseness parameters are required to fit the data. This result is an evidence for long range absorption mechanisms in ${}^6\text{He}$ induced reactions.

Keywords: Nuclear reaction ${}^{197}\text{Au}({}^6\text{He}, {}^6\text{He})$, ${}^{208}\text{Pb}({}^6\text{He}, {}^6\text{He})$, halo nucleus, Coulomb dipole polarizability, $E=4.5$ MeV/nucleon, optical potential.

PACS: 25.60.Dz, 25.60.Gc, 25.60.Bx, 21.10.Gv, 27.20.+n.

PACS numbers:

I. INTRODUCTION

The ${}^6\text{He}$ nucleus has a weakly bound three-body Borromean n-n- α structure and is known to have an extended two neutron distribution [1, 2]. Scattering of ${}^6\text{He}$ is therefore of considerable interest in nuclear physics since experiments may demonstrate sensitivity to this underlying exotic structure.

The interest of measuring elastic scattering of ${}^6\text{He}$ arises from the weakly bound nature of the projectile, which affects the dynamics of the collision. ${}^6\text{He}$ is bound by less than 1 MeV, so we expect that the coupling to the continuum can significantly modify cross sections in the elastic channel. Korshennikov et al. [3], reported on the measurement of proton elastic scattering by ${}^6\text{He}$, ${}^8\text{He}$ and ${}^{11}\text{Li}$.

One important aspect that we want to investigate is the role of Coulomb dipole polarizability [4, 5], which consists in the effect on the elastic channel of coupling to the break-up channels produced by the Coulomb dipole force. This effect has been investigated for the scattering of other weakly bound nuclei on heavy targets, such as $\text{d} + {}^{208}\text{Pb}$ [6], ${}^7\text{Li} + {}^{208}\text{Pb}$ [7], and ${}^{11}\text{Li} + {}^{208}\text{Pb}$ [8]. It is found that dipole polarizability gives rise to a significant reduction in the elastic scattering cross sections, which is particularly important for weakly bound nuclei. For the case of ${}^6\text{He}$ scattering on heavy targets, we expect that the strong Coulomb field generated by the target can distort the ${}^6\text{He}$ projectile, so that the ${}^4\text{He}$ core is pushed away from the target nucleus, while the neutrons in the halo remain unaffected.

Another significant aspect is the behaviour of the nuclear optical potential. It is an open question whether the optical model, using reasonable optical potentials, is an adequate approach to describe the elastic scattering of weakly bound nuclei. We are interested in determining the geometry and energy dependence of the optical potential obtained from a fit to the elastic cross sections, including the effect of dipole polarizability, and compare it with the optical potentials obtained for the most similar stable nucleus, which is ${}^6\text{Li}$. The elastic scattering of ${}^6\text{He}$ on ${}^{209}\text{Bi}$ has been measured in Notre Dame at energies near [9] and below [10] the Coulomb barrier. The analysis of the elastic scattering and reaction cross sections performed by the authors required the use of large, and energy-dependent, imaginary diffuseness parameters to reproduce the data. This result indicates the presence of a long range absorption mechanism, which could be related to the effect of Coulomb excitation.

We have presented in a previous publication the analysis of elastic scattering of ${}^6\text{He}$ on ${}^{208}\text{Pb}$ at 27 MeV, measured at Louvain la Neuve [13]. We found evidence that an extremely large diffuseness parameter was required to fit the data. This indicates that long range reaction mechanisms occur when ${}^6\text{He}$ was scattered on ${}^{208}\text{Pb}$. This is an important result, because it seems to indicate that the elastic scattering induced by exotic nuclei is qualitatively different from the scattering of stable nuclei. Nevertheless, it is important to confirm that this feature (the long range absorption) occurs when ${}^6\text{He}$ collides with other heavy targets. If this is the case, we could recognise long range absorption as a

robust feature of the scattering of ${}^6\text{He}$ at energies around the barrier, produced by its weakly bound structure, that does not depend strongly on the target properties.

In this work we present new experimental data of the quasi-elastic scattering of ${}^6\text{He}$ on ${}^{197}\text{Au}$ at 27 MeV. The $1/2^+$ state of ${}^{197}\text{Au}$ at 70 keV was not resolved from the $3/2^+$ ground state. We have explored the effect of including explicitly the excitation in a coupled channels calculation, and we find that the quasi-elastic differential cross sections (elastic plus inelastic) in the coupled channels calculation is very similar to the elastic differential cross section in an optical model calculation. The reason for it is that the flux going to the inelastic channels is subtracted from that of the elastic channel, leaving the quasi-elastic differential cross sections unaffected by the coupling.

We perform an analysis of the new set of data in parallel with the analysis of the data of ${}^6\text{He}$ on ${}^{208}\text{Pb}$ at the same energy. Our purpose is to search for evidence of long range absorption in these collisions.

II. EXPERIMENTAL SET-UP

The experiment was performed using the radioactive beam facility at the Cyclotron Research Centre at Louvain la Neuve in Belgium. The ${}^6\text{He}$ beam used in this experiment was produced via the ${}^7\text{Li}(p,2p){}^6\text{He}$ reaction using LiF powder target contained in a graphite holder [11].

The post-accelerated secondary ${}^6\text{He}$ beam of 27 MeV energy and intensity of 3×10^6 ions/s was scattered on a ${}^{197}\text{Au}$ target, which was in fact the backing of a ${}^7\text{LiF}$ target. The thickness of the ${}^{197}\text{Au}$ layer was approximately $300 \mu\text{g}/\text{cm}^2$. The thickness of the ${}^7\text{LiF}$ layer was $400 \mu\text{g}/\text{cm}^2$. The reaction products were detected in a detection system consisting of a LEDA and a LAMP type detector described in [12]. LEDA and LAMP silicon strip detector arrays cover two different angular ranges from 6° - 15° and from 23° - 72° in the laboratory frame, respectively. The details of the experimental setup has been described elsewhere [13].

Both the energy and the time of flight with respect to the cyclotron pulse were recorded for each reaction product. The in-beam energy resolution for silicon strip detectors was around 120-140 keV, depending on the scattering angle, which is mainly due to the beam emittance and beam straggling in the target. The timing information in connection with energy spectra enabled us to unambiguously identify the elastic scattering events.

The elastic scattering of ${}^6\text{He}$ from ${}^{197}\text{Au}$ could be readily separated from ${}^6\text{He}$ scattered from ${}^7\text{Li}$ and ${}^{19}\text{F}$ at angles greater than 10 degrees. Figure 1 shows the separation of elastic scattering events corresponding to ${}^{197}\text{Au}$ from those on ${}^7\text{Li}$ and ${}^{19}\text{F}$.

There is no evidence of break-up into ${}^4\text{He}$ at forward angles. At larger angles however there is some evidence for a broad break up component around $2/3$ of the elastic peak energy. In the present paper no attempt has been made to extract information on break up events, and only the elastic scattering events are investigated.

Only statistical uncertainties are considered in this analysis. The main source of systematic errors in our setup comes from possible uncertainties in the precise position of the LAMP array with respect to the target. This would lead to uncertainties in the scattering angle, which affect the ratio of the measured cross sections to Rutherford cross sections.

In a previous work [13] we found that this uncertainty in the position of LAMP affected mainly the relative normalisation of the small angles covered by LEDA and the large angles covered by LAMP. There, we found that minor changes in the positioning of LAMP (± 3 mm), affected the values of the long range absorption. As the small angles covered by LEDA only give information on the global normalisation, and this normalisation, for the intermediate angles (20 to 75 degrees) which are of interest, has systematic uncertainties, we have chosen in this work to neglect the data at small scattering angles, and adjust the normalisation of the LAMP data to the theoretical calculations.

We have also considered the effect of adding the number of counts measured in the different strips of the detector. Due to the geometry of LAMP array, we have six strips which correspond to the same nominal scattering angle. So, one could add the counts of all these strips, to reduce statistical uncertainties, as well as the number of data points. The result of applying this procedure is the ‘‘averaged data’’ set, shown in figure 2. This procedure is adequate to visualise the trend of the data. However, we consider that this procedure could hide the presence of some systematic uncertainties, related to the different solid angles of the sectors of the LAMP array, as well as the different scattering angles corresponding to the strips in different sectors, due to beam misalignment. So, we have also considered the ‘‘raw data’’ set, in which one experimental data point is associated to each strip. In the ‘‘raw data’’ set, the effect of beam misalignment is taken into account [13], so that the scattering angles corresponding to strips of different sectors are slightly different from the common nominal scattering angle. The set of data points so obtained, with more data and higher statistical uncertainties, are shown in figure 3. The statistical significance of fits to the ‘‘averaged data’’ set would be the same than that of the ‘‘raw data’’ set, if the difference in counting rates of the different sectors was purely statistical, and the difference between the actual scattering angle of each strip and the common nominal scattering angle was negligible. As this hypothesis is not necessarily true, we prefer to determine the optical

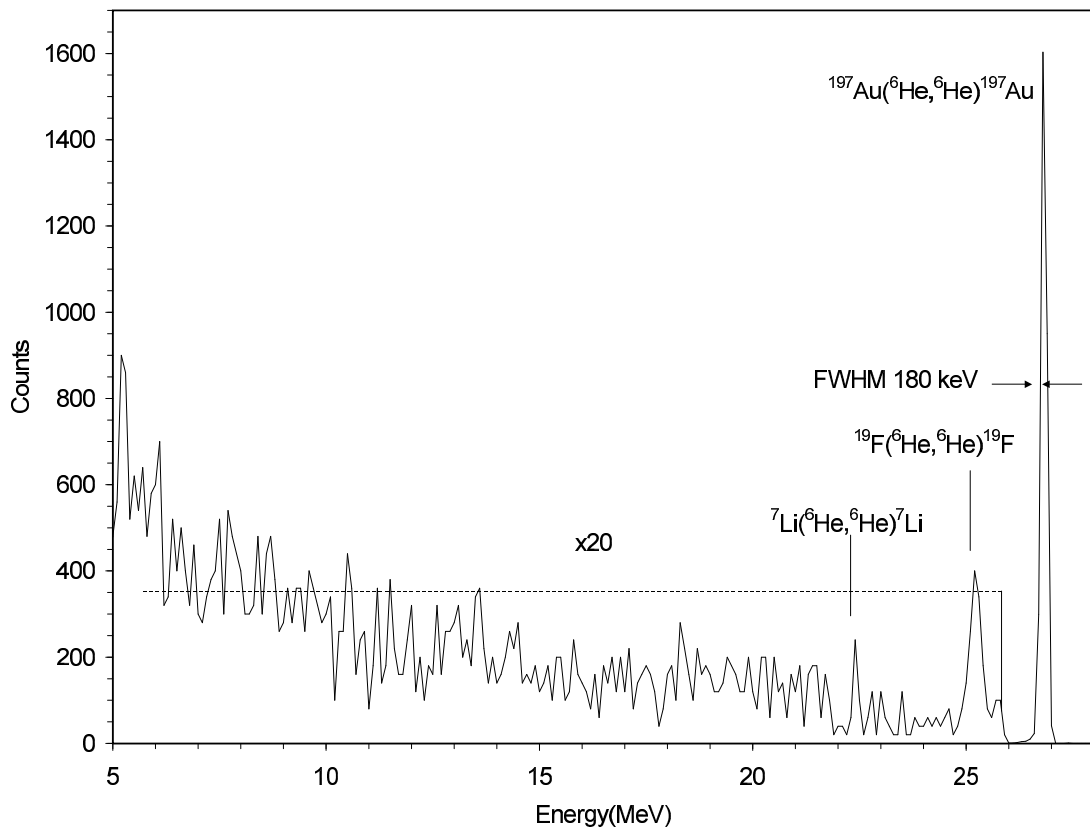


FIG. 1: The energy spectrum of 27 MeV ${}^6\text{He}$ scattered from ${}^7\text{LiF}(\text{Au})$ at $\theta_{lab}=27^\circ$

potential parameters from a χ^2 minimisation using the “raw data” set, which is directly related to the experimental measurements. However, to describe the qualitative features of the data is more adequate to use the “averaged data” of figure 2.

III. THEORETICAL CALCULATIONS

Dipole Coulomb excitation to break-up states can play an important role in the scattering of weakly bound nuclei. To describe the effect of this reaction mechanism in the elastic scattering, one can make use of a dynamic polarisation potential [4]. The form of the polarisation potential is obtained in a semi-classical framework requiring that the second order amplitude for the dipole excitation-deexcitation process and the first order amplitude associated with the polarisation potential are equal for all classical trajectories corresponding to a given scattering energy. This leads to an analytic formula for the polarisation potential for a single excited state [4]. The expression so obtained can be generalised for the case of excitation to a continuum of break-up states [5] giving rise to the following formula:

$$U_{pol}(r) = -\frac{4\pi Z_i^2 e^2}{9 \hbar v} \frac{1}{(r - a_o)^2 r} \int_{\epsilon_b}^{\infty} d\epsilon \frac{dB(E1, \epsilon)}{d\epsilon} \left(g\left(\frac{r}{a_o} - 1, \xi\right) + if\left(\frac{r}{a_o} - 1, \xi\right) \right) \quad (1)$$

where g and f are analytic functions defined as

$$f(z, \xi) = 4\xi^2 z^2 \exp(-\pi\xi) K''_{2i\xi}(2\xi z) \quad (2)$$

$$g(z, \xi) = \frac{P}{\pi} \int_{-\infty}^{\infty} \frac{f(z, \xi')}{\xi - \xi'} d\xi' \quad (3)$$

and $\xi = \frac{\epsilon a_o}{\hbar v}$ is the Coulomb adiabaticity parameter corresponding to the excitation energy ϵ of the nucleus.

Projectile	model	V (MeV)	W_{Pb} (MeV)	a_i (fm)	χ^2	σ_R^T (mb)	$\langle L \rangle_T$	σ_R^{dp} (mb)	$\langle L \rangle_{dp}$
${}^6\text{Li}$	Cook	109.5	22.38	0.884	—	—	—	—	—
${}^6\text{He}$	Fit W, a_i	109.5	7.16	1.70	139	1934	15.7	—	—
${}^6\text{He}$	DP ; Fit W, a_i	109.5	127.0	0.81	176	1713	14.9	302	26
${}^6\text{He}$	Fit V, W, a_i	81.0	7.00	1.75	119	1970	16.2	—	—
${}^6\text{He}$	DP ; Fit V, W, a_i	57.0	9.31	1.46	116	1878	16.2	318	24.9

TABLE I: Optical model parameters obtained from ${}^6\text{Li} + \text{A}$ (Cook systematics) and from ${}^6\text{He} + {}^{208}\text{Pb}$ data analysis performed in this work. The radial parameters are fixed, for the real and the imaginary potential to $r_{0r} = r_{0i} = 1.326$ fm and the real diffuseness parameter is fixed to $a_R = 0.811$ fm. The number of data points is 82. σ_R^T is the reaction cross section and σ_R^{dp} represents the reaction cross section due only to the dipole polarizability. $\langle L \rangle_T$ and $\langle L \rangle_{dp}$ are the respective average angular momentum weighted by the absorption cross section in each case.

When one compares the Coulomb dipole polarisation potentials for the collisions ${}^6\text{He} + {}^{208}\text{Pb}$, and ${}^6\text{He} + {}^{197}\text{Au}$, at the same energy of 27 MeV, one would expect that the larger charge of ${}^{208}\text{Pb}$ would produce larger dipole polarisation effects for ${}^6\text{He} + {}^{208}\text{Pb}$ than for ${}^6\text{He} + {}^{197}\text{Au}$ (note the factor Z_t^2 in eq. 1). However, the smaller charge of the ${}^{197}\text{Au}$ target also makes the adiabaticity parameter ξ smaller. This means that the imaginary part of the polarisation potential at long distances, describing long range absorption due to Coulomb break-up, is actually larger for ${}^{197}\text{Au}$ than for ${}^{208}\text{Pb}$.

The elastic differential cross sections are analysed assuming the validity of the optical model. The potential that describes the interaction between ${}^6\text{He}$ and ${}^{208}\text{Pb}$ is the sum of a monopole Coulomb potential, a dipole Coulomb polarisation potential and a phenomenological nuclear potential. The monopole Coulomb potential is determined by the charges of the colliding nuclei. Its only parameter is a Coulomb radius which, when taken in a reasonable range, does not affect significantly the cross sections. The dipole Coulomb polarisation potential describes the effect of coupling the ground state to break-up states in the continuum by the dipole Coulomb force. It is a complex, long range and energy dependent potential, which is completely determined from the values of the B(E1) distribution of ${}^6\text{He}$. The phenomenological nuclear potential includes the “direct” term of the nuclear interaction between ${}^6\text{He}$ and ${}^{208}\text{Pb}$ as well as the dynamic effects of nuclear coupling to break-up states, quadrupole Coulomb coupling and Coulomb-nuclear interference terms.

For our analysis we take theoretical values of the B(E1) distribution of ${}^6\text{He}$ [14, 15]. This determines completely the dipole Coulomb polarisation potential. The real part of the dipole polarization potential is plotted as the dashed-dotted line in Fig. 6, while the imaginary polarization potential is plotted as the dashed line in Fig 5. For the nuclear potential, as a starting point, we use a Woods-Saxon potential, which was obtained from the optical model analysis of elastic scattering of ${}^6\text{Li}$, in mass range of 24-208 and energy range of 13-156 MeV [16]. We shall refer to this potential as “Cook” potential. The optical model parameters used are given in table 1.

Our starting consideration is that ${}^6\text{Li}$ and ${}^6\text{He}$ have similar structures, and both are weakly bound (by 1.475 MeV and 0.975 MeV, respectively). So, the main qualitative difference between them could be that the dipole Coulomb force can break up ${}^6\text{He}$ into ${}^4\text{He} + 2n$, but it cannot break up ${}^6\text{Li}$ into ${}^4\text{He} + {}^2\text{H}$. The dipole Coulomb operator, in an $N = Z$ nucleus, is an isospin 1 operator. Since ${}^6\text{Li}$, ${}^4\text{He}$ and ${}^2\text{H}$, have isospin 0 in their ground states, it is not possible that the dipole Coulomb force breaks up ${}^6\text{Li}$ into ${}^4\text{He} + {}^2\text{H}$.

This difference between ${}^6\text{Li}$ and ${}^6\text{He}$ is explicitly taken into account by means of the dipole Coulomb polarisation potential. In figure 2 we present the “averaged data” measured for the collision of ${}^6\text{He}$ on ${}^{197}\text{Au}$ and ${}^{208}\text{Pb}$ at 27 MeV bombarding energy. The solid lines are the global optical model calculations which uses Cook potential [16]. These calculations, that do not take into account the effect of dipole polarizability, show a well defined rainbow around 43 degrees, which is clearly absent from the experimental data. The calculations including dipole polarizability (dotted lines) also show a rainbow, but it is less pronounced and it appears at a smaller angle. So, we can conclude that the effect of dipole polarizability is clearly visible in the scattering of ${}^6\text{He}$ on ${}^{197}\text{Au}$ and ${}^{208}\text{Pb}$ at 27 MeV, and explains in part the disappearance of the rainbow in the experimental data. However, it is also clear that the optical potential obtained from ${}^6\text{Li}$ scattering (Cook potential), even supplemented with the Dipole Polarisation Potential, is not adequate to reproduce the scattering of ${}^6\text{He}$ on ${}^{197}\text{Au}$ and ${}^{208}\text{Pb}$ at 27 MeV.

We now proceed to modify Cook ${}^6\text{Li}$ optical potential to fit the ${}^6\text{He}$ scattering data. The first argument is that the reaction channels produced by ${}^6\text{He}$ scattering (mostly break-up and neutron transfer), will be different from those of ${}^6\text{Li}$. These reaction channels affect mainly the imaginary part of the potential, which describes the loss of flux from the elastic channel. So, we allowed the depth and the diffuseness of the potential to vary. The results of these calculations are shown in tables I and II. The fit of the data is fair, but not perfect, as it can be seen from the values of χ^2 . If the value of the depth of the real potential is also fitted, then the fit of the data is very good, as it is shown in tables I and II, as well as in figure 3.

Projectile	model	V (MeV)	W_{Au} (MeV)	a_i (fm)	χ^2	σ_R^T (mb)	$\langle L \rangle_T$	σ_R^{dp} (mb)	$\langle L \rangle_{dp}$
${}^6\text{Li}$	Cook	109.5	22.65	0.884	—	—	—	—	—
${}^6\text{He}$	$a_i({}^{208}\text{Pb})$; Fit W,	109.5	6.20	1.70	135	1880	15.5	—	—
${}^6\text{He}$	DP ; $a_i({}^{208}\text{Pb})$; Fit W	109.5	84.3	0.81	141	1835	16.8	523	28.1
${}^6\text{He}$	V, $a_i({}^{208}\text{Pb})$; Fit W	81.0	6.12	1.75	113	1911	15.8	—	—
${}^6\text{He}$	DP ; V, $a_i({}^{208}\text{Pb})$; Fit W	57.0	6.36	1.46	111	1907	17.6	564	26.6

TABLE II: Optical model parameters obtained from ${}^6\text{Li} + \text{A}$ (Cook systematics) and from ${}^6\text{He} + {}^{208}\text{Pb}$ data analysis according to table I applied to ${}^6\text{He} + {}^{197}\text{Au}$ angular distributions. The only fitted parameter is W_{Au} which is the depth of the imaginary potential to fit ${}^6\text{He} + {}^{197}\text{Au}$ data. The number of data points is 80.

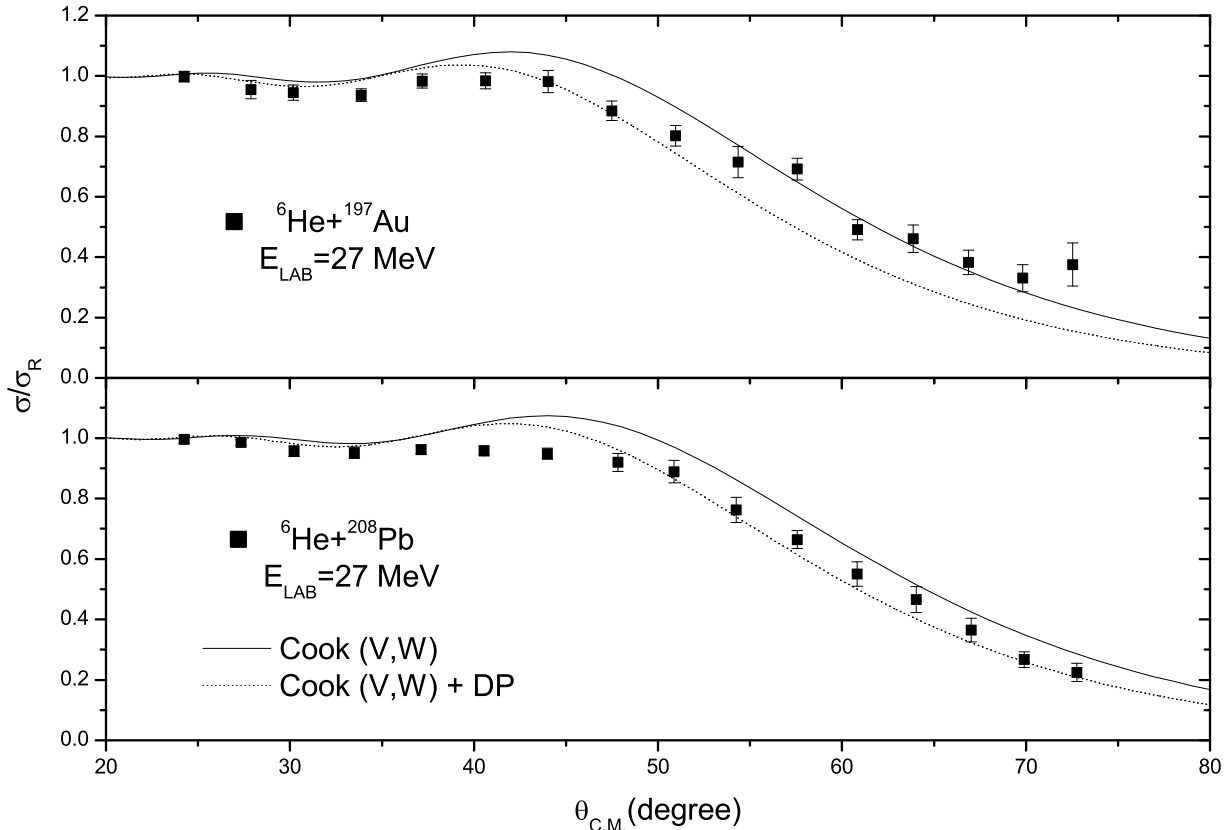


FIG. 2: Elastic scattering angular distribution of ${}^6\text{He} + {}^{197}\text{Au}$, ${}^{208}\text{Pb}$ at 27 MeV. Data are “averaged data” (see text). The lines are optical model calculations, without (solid line) and with (dashed line) taking into account dipole polarizability, which uses the same potential (real and imaginary) that fits ${}^6\text{Li}$ systems (for details, see table I).

In fitting the data, we have taken into account that the data of ${}^6\text{He}$ on ${}^{208}\text{Pb}$ are much more accurate than those of ${}^6\text{He}$ on ${}^{197}\text{Au}$. So, whenever possible, we kept the same parameters for the two targets. We only allowed to vary the depth of the imaginary potential, because the targets ${}^{208}\text{Pb}$ and ${}^{197}\text{Au}$ could lead to different reaction channels. The parameters that fit the experimental data of the reaction ${}^6\text{He}$ on ${}^{197}\text{Au}$, shown in table II are similar to those obtained for the reaction ${}^6\text{He}$ on ${}^{208}\text{Pb}$, shown in table I. So are the values of χ^2 obtained in the best fits. We can conclude that both sets of data give a consistent message, indicating the presence of long range reaction mechanisms.

It is interesting to comment on the values of the reaction cross sections obtained in the fits. These are around 1900 mb in all the calculations that fit accurately the elastic data. From the reaction cross sections, we have extracted the contribution due to the imaginary part of the Coulomb polarisation potential. This value is an estimate of the

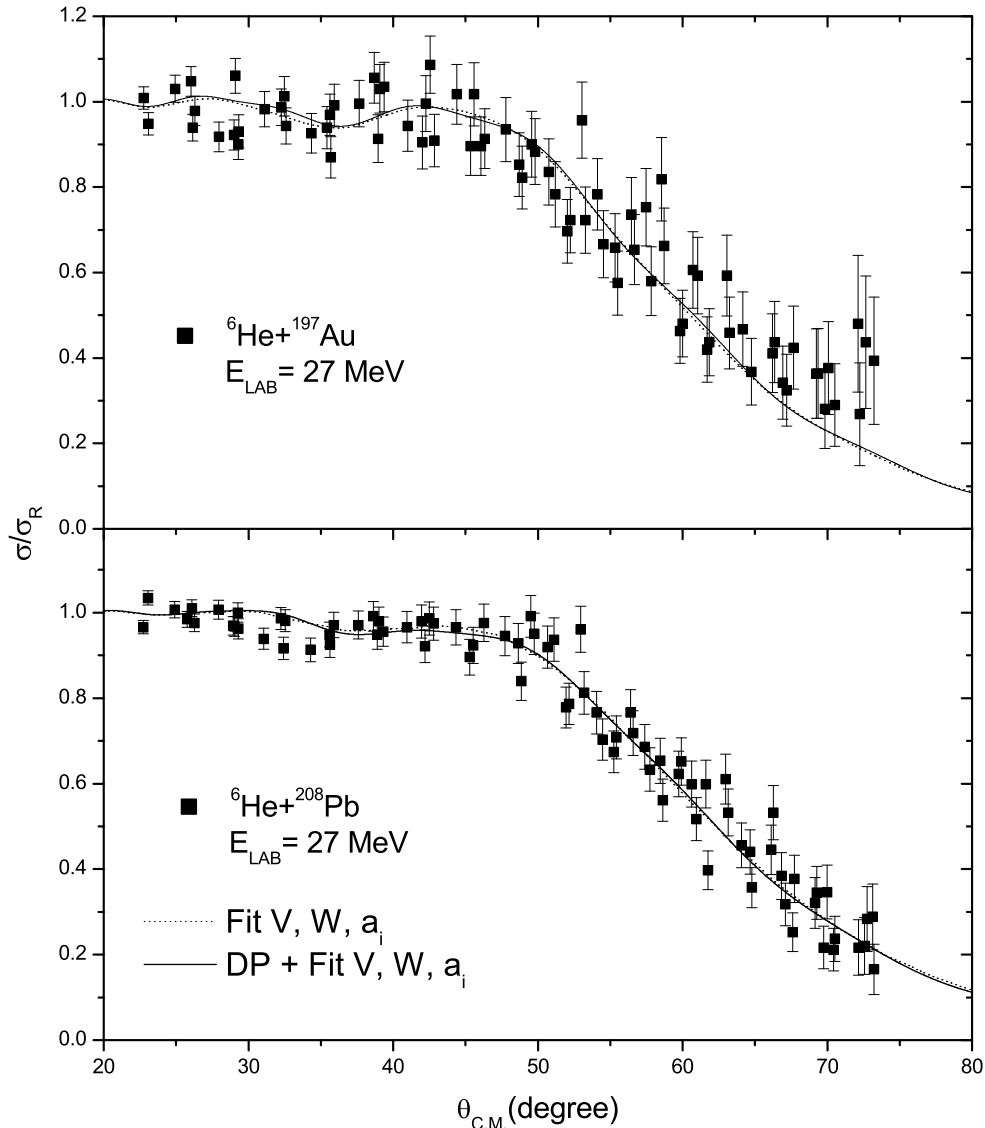


FIG. 3: Elastic scattering angular distribution of ${}^6\text{He} + {}^{197}\text{Au}$, ${}^{208}\text{Pb}$ at 27 MeV. Data are “raw data” (see text). The full line is an optical model calculation using Cook parameters with a reduced depth of real potential ($V = 81\text{MeV}$). The dashed line includes dipole polarizability effects and a reduced depth of real potential ($V = 57\text{MeV}$). The parameters (W , a_i) of the imaginary potential were also searched for a minimum χ^2 in each calculation.

reaction cross section which is due to Coulomb break-up. Note that this value is 318 mb for the ${}^{208}\text{Pb}$ target, and 564 mb for the ${}^{197}\text{Au}$ target. Naively, one would expect that the target with higher charge would induce more Coulomb break-up. However, the lower charge of ${}^{197}\text{Au}$ makes the energy of the collision (27 MeV) higher with respect to the Coulomb barrier, reducing the collision time, and thus producing more Coulomb break-up. Also, it should be mentioned that Coulomb break-up leads indeed to long range absorption. This can be seen from the values of $\langle L \rangle_{dp}$, which is the average L-value of the reaction cross sections due to coulomb excitation. They are considerably larger than the values of $\langle L \rangle_T$, which is the average L-value of the total reaction cross sections.

The results of the optical model fits discussed above, which have been performed with the code FRESKO [17], are shown in figure 3, and the sets of optical model parameters are shown in table I (${}^{208}\text{Pb}$) and table II (${}^{197}\text{Au}$). We have also performed calculations varying the value of a_i , and fitting the value of W for each a_i . The values of χ^2/n for these fits are plotted in Figure 4. The data on the ${}^{208}\text{Pb}$ target indicate clearly the need for large imaginary

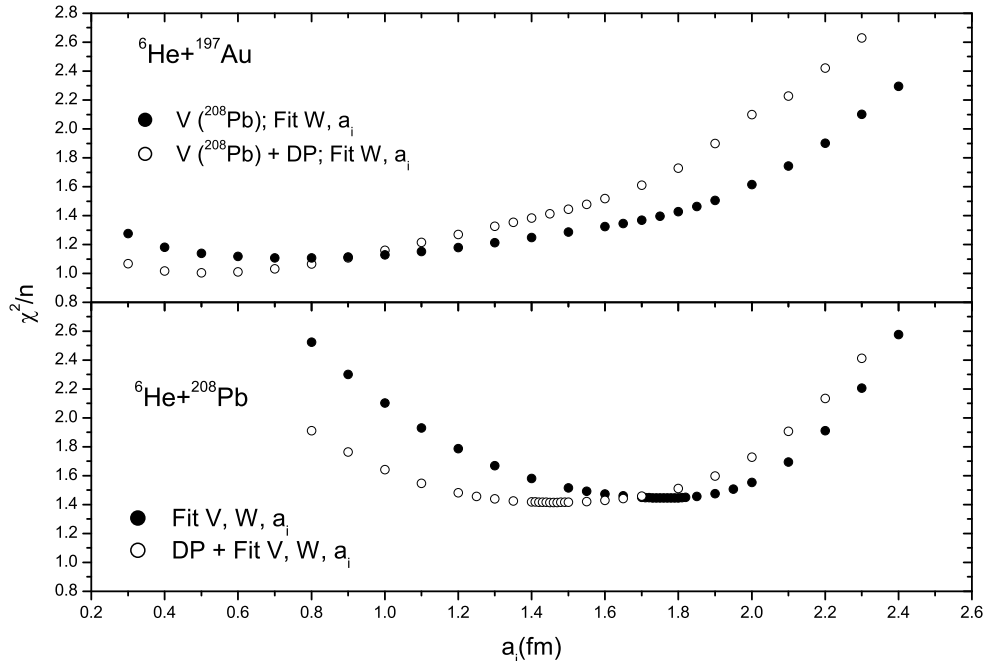


FIG. 4: Reduced χ^2 for various values of imaginary depth and diffuseness (W , a_i) parameters, using the best real depth (V) without (closed symbols) and with (open symbols) the inclusion of the dipole polarisation potential, for the collision of $^6\text{He} + ^{197}\text{Au}$, ^{208}Pb .

diffuseness parameters, to obtain good fits $\chi^2/n \leq 1.5$. However, the data on the ^{197}Au target can be fitted with the same accuracy with almost any diffuseness parameter. This is an effect of the larger statistical uncertainties of the ^{197}Au data. In any case, we can say that the large imaginary diffuseness parameter required to reproduce the data on the ^{208}Pb target is not inconsistent with the values required to reproduce the data on the ^{197}Au target. Also, the fits show that the explicit inclusion of the Dipole Polarisation Potential reduce the values of the diffuseness parameters required to fit the data in both cases.

The fits presented in tables I and II, and in figure 4 make use of the “raw data” set, which are shown in figure 3. We have also performed the optical potential fits making use of the “averaged data” set, presented in figure 2. We find that the results for the potentials that produce the best fits are very similar in both cases. This indicates that, in these experiments, there were not systematic differences between the cross sections obtained from the detector strips of the different sectors, and that the difference between actual and nominal scattering angles was not important, for the observable considered.

IV. DISCUSSION

One objective of this analysis is to investigate if, as suggested in our previous paper [13], there are evidences of long range mechanisms that lead to the loss of flux in the elastic channel at kinematic conditions that suggest the nuclei are far beyond the strong absorption radius, which, in our case, is approximately $R_{SA} = 11.5\text{fm}$ for both targets.

The other objective is to investigate the role of coulomb dipole polarizability in the scattering of this weakly bound, and hence easily polarizable, nucleus.

A. Evidence for long range absorption mechanisms

The first evidence for the long range absorption comes from the values of the imaginary diffuseness parameters required to fit the data. The plot of χ^2 (figure 4), for the $^6\text{He} + ^{208}\text{Pb}$, clearly indicates that the imaginary potential

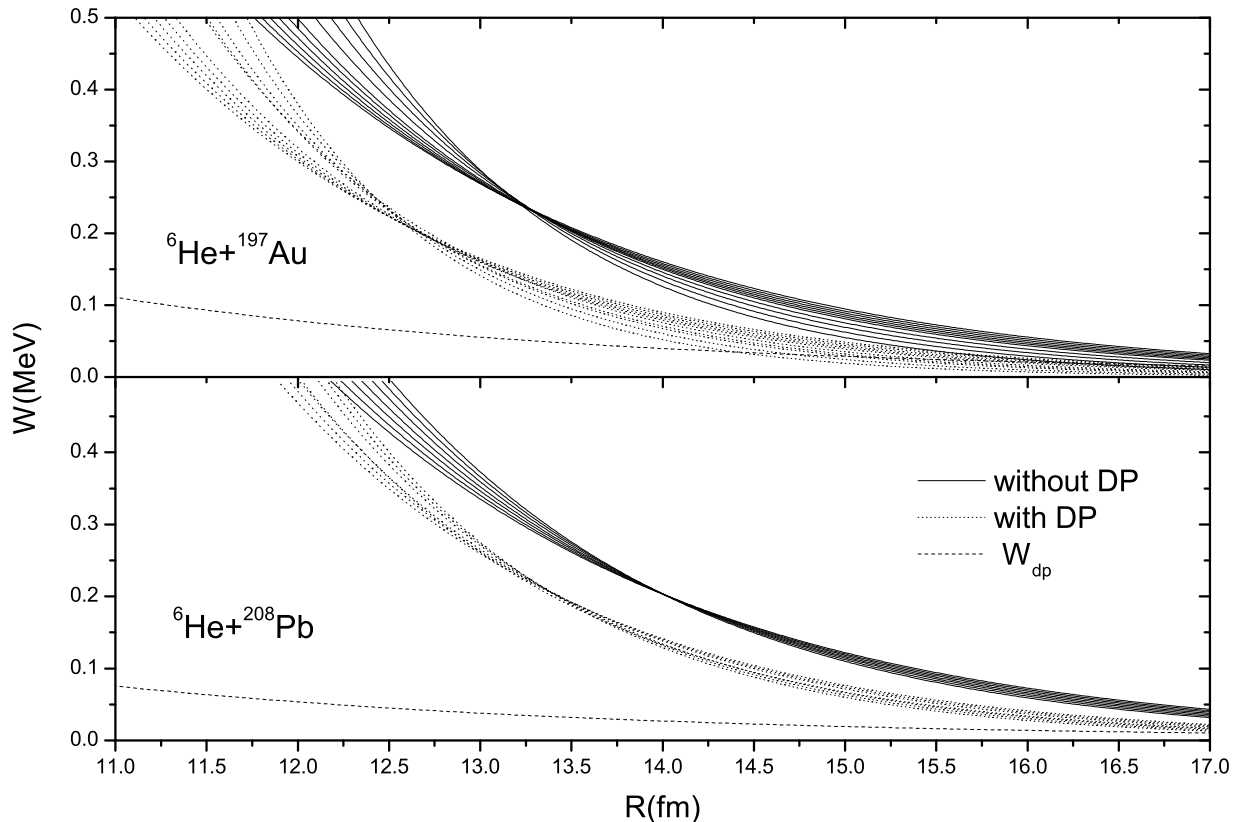


FIG. 5: Imaginary potentials that fit the data, including (dotted lines) and not including (solid lines) the dipole polarisation potential, as a function of the interacting distance. For the ${}^6\text{He} + {}^{208}\text{Pb}$ case, we took $a_i = 1.30 - 1.90$ fm. For the ${}^6\text{He} + {}^{197}\text{Au}$ case, we took $a_i = 0.80 - 1.90$ fm. The dashed line represent the imaginary part of the dipole polarisation potential.

needed to fit the data has a diffuseness considerably larger than that of the real potential. A diffuseness parameter in the range of 1.30 to 1.90 fm is needed to fit the data. This is to be compared to the value of the diffuseness of the real potential, which is $a_r = 0.811$ fm. We point out that this diffuseness is not as large as the one found in the previous work [13], but there the diffuseness of the real potential was allowed to vary, and it also acquired large values. The systematics of our calculations show that the imaginary potential has to be much more diffuse than the real potential to reproduce the data.

The second evidence for the long range absorption comes from the relatively large values of the average reaction angular momenta $\langle L \rangle_T$. In a cutoff model, which is not unreasonable to describe the absorption in heavy ion collisions, the absorption is maximum for $L + 1/2 < \lambda$ and negligible for $L + 1/2 > \lambda$. The relation of the cutoff parameter λ and the reaction cross section is given by [18] $\sigma_R = \pi\lambda^2/k^2$. Then, in this sharp cutoff model, $\langle L \rangle_T + 1/2 = 2/3\lambda$. The values of the reaction cross sections in these reactions (see tables I,II) are about 1900 mb. This leads to values of $\langle L \rangle_T \simeq 13.5$, which is considerably smaller than the values shown in the table. This is an indication of the fact that the reaction cross sections extend to up to values of L which are well beyond the grazing angular momentum.

The third evidence for the long range absorption comes from the values of the imaginary potential. In figure 5 different families of imaginary potentials which fit reasonably the data are plotted as a function of the distance. Let us focus on the solid lines, which correspond to optical model calculations in which the dipole polarisation potential (DPP) is not explicitly included. We see that the lines cross at 13.25 fm (Au) and 14.0 fm (Pb). This indicates the region of sensitivity to the imaginary potential. Note also that the imaginary potential still has sizeable values at distances as large as 16 fm. In figure 6 we present real potentials that fit the data. These potentials cross between 11 and 12 fm, which is the region of the strong absorption radius (11.5 fm). So, we see that while the real potential is determined around the distance of the strong absorption radius, the imaginary potential is determined at much

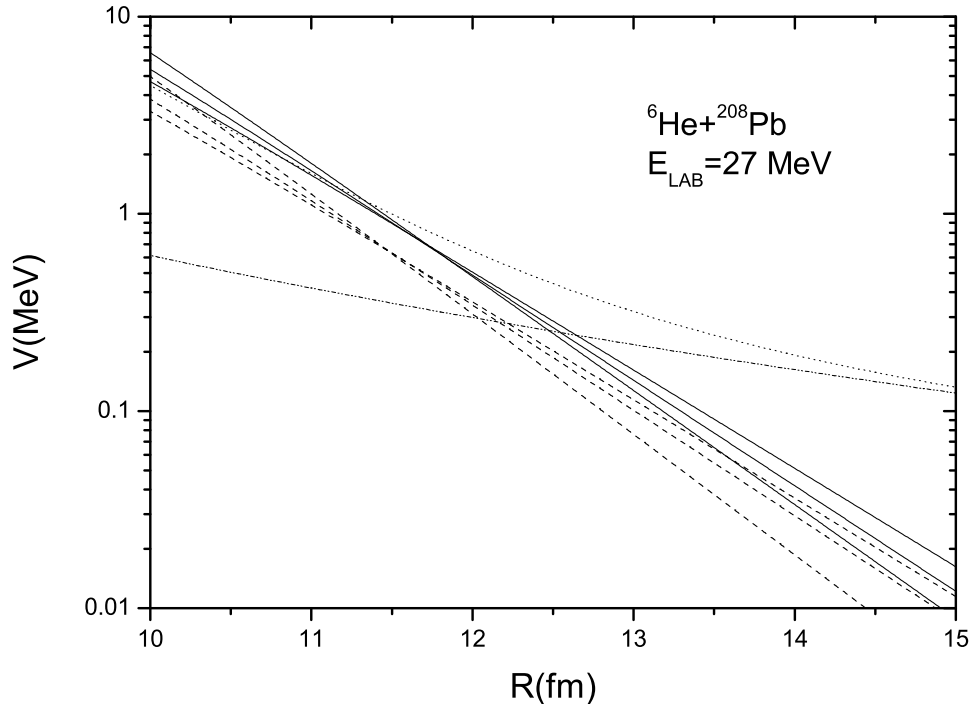


FIG. 6: Real potentials that fit the data including (dashed lines) and not including (solid lines) the dipole polarisation potential, as a function of the interacting distance. The central line is the best fit, and the other lines are obtained varying slightly the diffuseness parameter, and readjusting the potential depth. The dashed-dotted line is the real part of the DPP due to dipole polarizability. The dotted line is the sum of the real potential, including DPP, plus the real part of the DPP. This calculation agrees with the calculations performed without including explicitly a DPP (solid lines), to the strong absorption radius $R_{SA} = 11.5$ fm

larger distances. This point should be taken into account when investigating the energy dependence of the real and imaginary optical potentials of exotic nuclei.

It should be noticed that these evidences for long range absorption are deduced from a consistent analysis of the scattering data on ^{197}Au and ^{208}Pb targets. The data on the ^{197}Au target, considered separately, are not sufficiently accurate to determine unambiguously the depth and diffuseness of the imaginary potential. However, the other two evidences for long range absorption (large values in the average reaction angular momenta, and sensitivity of the imaginary potential to large distances) come out clearly from the analysis of the ^{197}Au data. These features are unaffected by the ambiguities of the imaginary potential parameters, as shown in figure 5.

B. Role of Coulomb dipole polarizability

Having established the presence of long range reaction mechanisms, we will now discuss the relevance of the Coulomb dipole polarizability in this mechanism. For that purpose, we will consider the calculations in which the DPP is explicitly included. In these calculations, the phenomenological imaginary potential describes the absorption produced by dynamical effects different from pure dipole Coulomb excitation.

First, we investigate the change in the values of the imaginary diffuseness parameters. As shown in table I, the value of the diffuseness parameter when the DPP is explicitly included is 1.46 fm, to be compared with 1.75 fm when it was omitted. This can also be seen in figure 4, where the values of the diffuseness parameters which reduce the values of χ^2 are definitively smaller when the DPP is included. Note that in the χ^2 plot for $^6\text{He} + ^{197}\text{Au}$, the relevant magnitude is not the absolute minima. In the case of $^6\text{He} + ^{208}\text{Pb}$, the best fits obtained had $\chi^2/n \simeq 1.5$. We can argue that, for the less accurate $^6\text{He} + ^{197}\text{Au}$ data, a fit with $\chi^2/n \leq 1.5$ already indicates a good fit of the data.

Hence, the plots should be interpreted saying that, when the DPP is not explicitly included, the imaginary diffuseness parameter should be less than 1.90 fm, while if the DPP is explicitly included, it should be less than 1.60 fm. This is compatible with the values obtained with the ${}^6\text{He} + {}^{208}\text{Pb}$ data. The data therefore indicate that when the DPP is included, there is a need of long range imaginary potentials, but the range is not as large as when the DPP is not included.

Second, we investigate the values of the reaction cross sections and average L-values produced by the DPP. As shown in tables I, II, a significant fraction of the reaction cross section is due to the coulomb dipole excitation mechanism. In addition, the values of the average angular momenta are very large (24.4 and 26.6 respectively for the ${}^{197}\text{Au}$ and ${}^{208}\text{Pb}$ targets). These values of the angular momenta correspond to distances of closest approach of 14.6 and 14.8 fm, which are well beyond the strong absorption radius. This indicates that coulomb dipole polarizability is indeed a mechanism that generates long range absorption. This produces a reduction of the elastic cross sections at forward angles, which is associated with the disappearance of the rainbow previously discussed. It should be noticed that the absorption cross section due to the effect of dipole polarizability does not increase with the charge of the target. This is due to the effect of the adiabaticity parameter ξ , which is larger for the ${}^{208}\text{Pb}$ target than for the ${}^{197}\text{Au}$ target. This means that, although the coulomb dipole force is weaker in the ${}^{197}\text{Au}$ target, it is more effective in producing break-up cross sections, which generate absorption in the elastic channel.

Third, we investigate the values of the potentials as a function of the distance. Consider the dashed lines in figure 5. They represent the imaginary potentials which describe absorption by mechanisms different from the dipole polarizability. They cross at distances of 12.5 (Au) and 13.25 (Pb) fm, which are considerably smaller than the crossings of the full lines, where the DPP is not explicitly considered. So, we see explicitly that a long range absorption mechanism is required in addition to the pure dipole coulomb excitation. However, the range of the imaginary potential associated to this additional mechanism is not as large as the imaginary DPP, which is shown by the dotted line.

The DPP has a real component, attractive, which is shown by the dot-dashed line. This potential has a very long range, but its effect on the scattering is determined mainly by its value at the strong absorption radius. As shown in figure 6, all the calculations that fit the data, either with or without the explicit inclusion of the DPP, have values of the real potential which are about 0.90 MeV at 11.5 fm. However, the long range attraction enhances the absorption by the imaginary potentials. This explains that the sum of the DPP imaginary potential and the phenomenologic potentials given by the dashed lines in figure 5 are smaller than the full lines, which represent the phenomenologic imaginary potentials where DPP is not considered.

We can conclude that the effect Coulomb Dipole Polarizability accounts for an important fraction of the long range absorption needed to describe the elastic scattering of ${}^6\text{He}$ on ${}^{208}\text{Pb}$ and ${}^{197}\text{Au}$ at 27 MeV. However, other reaction mechanisms such as nuclear break-up, coulomb-nuclear interference effects or neutron transfer to bound or unbound states can play also an important role.

We consider that a proper understanding of the long range absorption is required. The use of nuclear reactions as an spectroscopic tool to investigate the structure of exotic nuclei requires a deep understanding of the reactions induced by exotic nuclei. This work indicates that simple preconceptions based on the experience of the optical model on stable nuclei, such as the role of the strong absorption radius, are not extrapolatable to the scattering of exotic nuclei.

Experimental measurements of the elastic scattering of ${}^6\text{He}$ and other exotic nuclei on a variety of targets, along with the measurement of the main reaction channels, would be required. Reaction calculations with a proper treatment of the break-up channels would be needed to understand the role of absorption.

Acknowledgements:

The authors thank the staff at the Cyclotron Research Centre accelerator facility in Louvain-la-Neuve, Belgium, for providing us with an intense and good quality radioactive beam. ORK acknowledges a grant from the Iranian government and support from the University of Sevilla for his stay at this university. PJW, TD, ACS, AL, ADP and WBS would like to acknowledge support from the British EPSRC. AMSB, IMB, MVA, AM, MAGA and JGC would like to acknowledge support from the Spanish MCyT under projects FPA2003-05958 and FPA2005-04460. AMSB acknowledges a research grant from the Spanish MCyT.

-
- [1] I. Tanihata, J. Phys. G **22** (1996) 157.
 - [2] P. G. Hansen, B. Jonson, Europhysics Letter **4** (1987) 409.
 - [3] A. A. Korshennikov *et al.*, Nucl. Phys. A **616** (1997) 189c.
 - [4] M. V. Andrés, J. Gómez-Camacho and M. A. Nagarajan, Nucl. Phys. A **579** (1994) 273.
 - [5] M. V. Andrés, J. Gómez-Camacho and M. A. Nagarajan, Nucl. Phys. A **583** (1995) 817.

- [6] A. M. Moro *et al.*, Nucl. Phys. A **648** (1999) 141.
- [7] I. Martel *et al.*, Nucl. Phys. A **641** (1998) 188.
- [8] M. V. Andrés and J. Gómez-Camacho, Phys. Rev. Lett. **82** (1999) 1387.
- [9] E.F. Aguilera *et al.*, Phys. Rev. Lett. **84** (2000) 5058.
- [10] E.F. Aguilera *et al.*, Phys. Rev. C **63** (2001) 061603R.
- [11] J. Vervier, Nucl. Phys. A **616** (1997) 97c.
- [12] T. Davinson *et al.*, Nucl. Instr. and Meth. A **454** (2000) 350.
- [13] O.R. Kakuee *et al.*, Nucl. Phys. **A728** (2003) 339-349.
- [14] B.V. Danilin, I.J. Thompson, M.V. Zhukov and J.S. Vaagen, Nucl. Phys. **A632** (1998) 383-416.
- [15] I.J. Thompson, B.V. Danilin, V.D. Efros, J.S. Vaagen, J.M. Bang and M.V. Zhukov, Phys. Rev. C **61**, 24318 (2000)
- [16] J. Cook, H. J. Gils, H. Rebel, Z. Majka and H. Klewe-Nebenius Nucl. Phys. **A388** (1982) 173-186.
- [17] I. J. Thompson, Comput. Phys. Rep **7**, 167 (1988).
- [18] G. R. Satchler, Direct Nuclear Reactions, Oxford University Press, 1983, Oxford.